Non-LTE Effects in Inertial Confinement Fusion Target Chambers

J.J. MacFarlane, G.A. Moses, R.R. Peterson

April 1988

UWFDM-761

Nucl. Fusion 29 (1989) 27.

FUSION TECHNOLOGY INSTITUTE

UNIVERSITY OF WISCONSIN

MADISON WISCONSIN

Non-LTE Effects in Inertial Confinement Fusion Target Chambers

J.J. MacFarlane, G.A. Moses, R.R. Peterson

Fusion Technology Institute
University of Wisconsin
1500 Engineering Drive
Madison, WI 53706

http://fti.neep.wisc.edu

April 1988

UWFDM-761

Nucl. Fusion 29 (1989) 27.

NON-LTE EFFECTS IN INERTIAL CONFINEMENT FUSION TARGET CHAMBERS

J.J. MacFarlane, G.A. Moses, R.R. Peterson

Fusion Technology Institute
1500 Johnson Drive
University of Wisconsin - Madison
Madison, Wisconsin 53706

April 1988

UWFDM-761

Submitted to Nuclear Fusion for publication.

ABSTRACT

The equation of state and radiative properties of high temperature, low-to-moderate density ($\lesssim 10^{21}$ cm^{-3}) plasmas are studied in order to determine the conditions for which non-LTE effects become important, and to assess the importance of non-LTE processes in target chambers during high yield inertial fusion target explosions. This is accomplished by considering both 3-body (collisional) and 2-body (radiative and dielectronic) recombination and de-excitation processes in calculating the steady-state ionization and excitation populations. Our results indicate that non-LTE processes generally become important at temperatures $\gtrsim$ 1, 10 and 100 eV for plasma densities of 10^{18}, 10^{19}, and 10^{21} cm^{-3}, respectively. Radiation-hydrodynamic simulations utilizing the equation of state and opacities for a non-LTE argon plasma were performed to study the response of a background gas to an inertial fusion target explosion. Our calculations indicate that non-LTE processes are often the dominant atomic processes in the background plasma, and can strongly affect the radiative and shock properties as energy is transported away from the point of the target explosion.

1. INTRODUCTION

Inertial confinement fusion (ICF) target explosions are expected to release several hundred megajoules of energy in the form of neutrons, x-rays, and energetic ions [1]. Transporting the energy from the ICF driver (laser, light ion, or heavy ion) to the target will likely necessitate the presence of a backgound gas of density ~ 10^{12} to 10^{18} atoms/cm^3 [2]. An additional important benefit of a background gas is that it can prevent the target x-rays and ions from inflicting unacceptable damage to the cavity surroundings, such as the target chamber first wall or diagnostic equipment [3]. A relatively dense background gas will absorb the x-rays and ions, creating a hot (T ~ 10^3 eV) microfireball which rapidly expands and generates a strong shock (see Figure 1). Under these circumstances, the target energy is transported to the outer regions of the chamber primarily by two mechanisms: (1) reradiated photons from the background plasma, or "thermal radiation", and (2) hydrodynamic expansion of the blast wave. The manner in which energy is partitioned between these two mechanisms strongly depends on the radiative properties of the background plasma.

Understanding the energy transport away from the target is critical for two reasons. First, if a substantial amount of energy is transported hydrodynamically, the shock-produced impulse could potentially cause structural damage to the chamber wall. Second, the wall will experience a large heat flux which in turn could cause substantial vaporization of the wall material if the background plasma emission rate is sufficiently high. Large amounts of vaporized wall material may be unacceptable for several reasons: (1) the condensation time may restrict the repetition rate of ICF reactors [4], which are typically proposed to be ~ 1 to 10 explosions per second [5]; (2) the

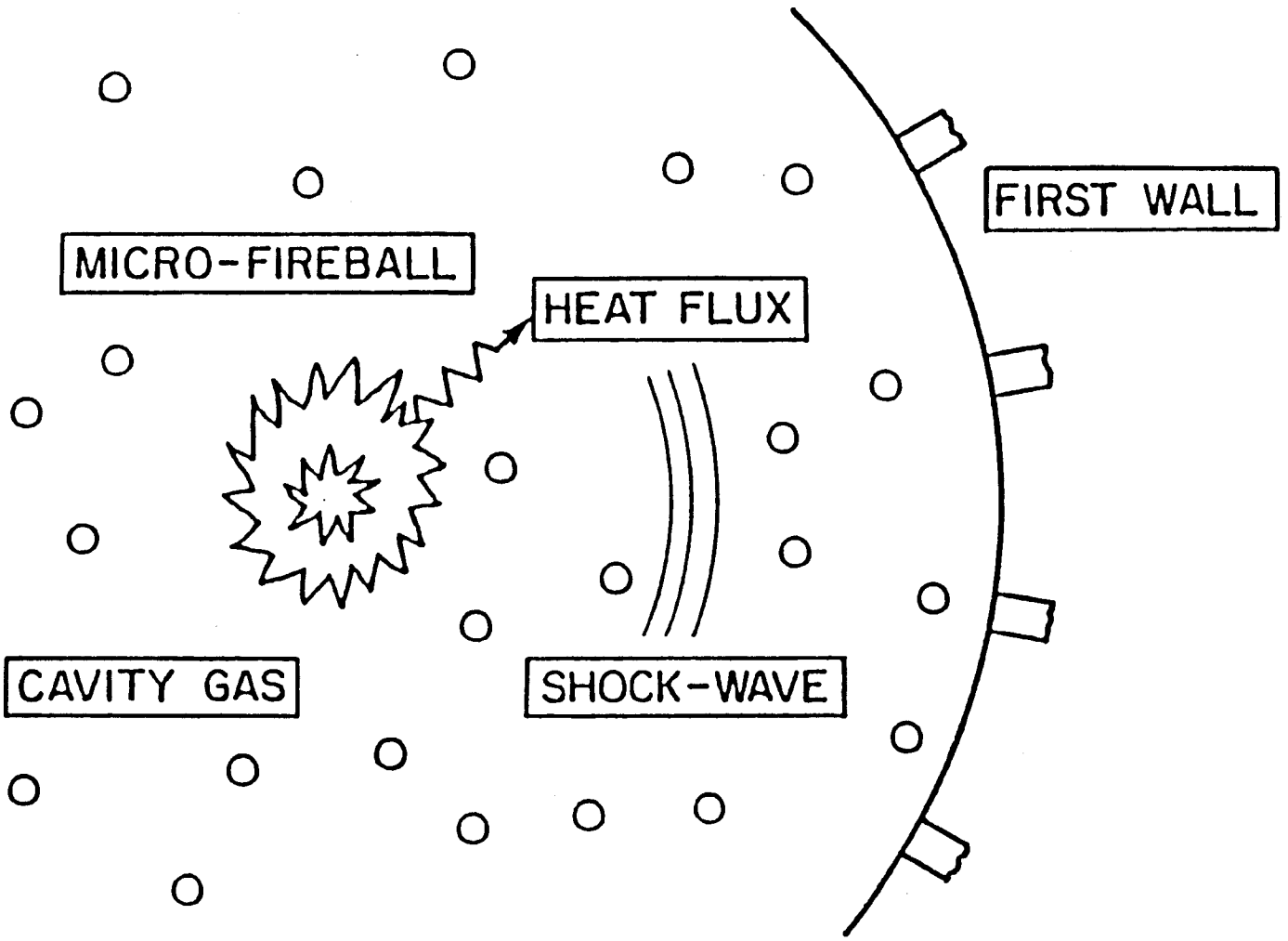

Fig. 1. Schematic diagram showing the physical processes occurring in an inertial fusion target chamber after the target explodes.

erosion rate may be excessive; and (3) the recoil may cause structural damage to the wall. Thus, it is important to determine how the energy originating from the target x-rays and ions is ultimately deposited at the chamber wall.

In previous studies of transport processes in ICF target chambers [6,7], the radiative properties of the background plasma were calculated under the assumption of local thermodynamic equilibrium (LTE). For the LTE assumption to be valid, the plasma density must be sufficiently high that all atomic processes -- ionization, recombination, excitation, and deexcitation -- are collisionally dominated [8]. However, this assumption is not always valid for conditions that occur in ICF chambers. In fact, it is rarely true when the background gas (room temperature) pressure is $\lesssim$ 1 torr because the radiative deexcitation and recombination rates exceed the collisional rates. At somewhat higher gas pressures, ~ 10 - 100 torr, the plasma can migrate between the collisionally dominated, LTE regime and the radiatively dominated, non-LTE regime as it heats up and later cools. Therefore, both collisional and radiative processes must be simultaneously considered in calculating the radiative properties of ICF target chamber plasmas.

The purpose of this paper is to identify the conditions for which the assumption of local thermodynamic equilibrium breaks down, and to illustrate how using the more appropriate non-LTE plasma radiative properties affects the radiative and hydrodynamic transport of energy away from the target. The plasma properties are computed by considering both radiative and collisional processes in calculating the ionization and excitation populations, as well as the absorption and emission coefficients. The details of calculating the plasma properties are discussed in Section 2.

In Section 3, we present results of radiation-hydrodynamic calculations for typical ICF high yield target chamber environments using the plasma properties calculated in Section 2. Here, we will primarily examine the radiative flux and shock-produced impulse at the chamber wall, and show how the more general non-LTE plasma results differ from those of LTE plasmas. And finally, we will review the conclusions of this study in Section 4.

2. PLASMA PROPERTIES

The steady-state ionization and excitation populations of the background plasma are calculated using detailed balancing arguments [9]. The fraction of ions in each ionization state is determined by equating the number of collisional ionizations with the sum of collisional, radiative, and dielectronic recombinations. Similarly, the excitation populations are calculated by balancing the number of collisional excitations with the total number of collisional and radiative deexcitations. Radiative contributions to excitation and ionization can be ignored because the radiation energy density in ICF target chambers is small.

A detailed description of the assumptions and physical processes considered in our calculations of the plasma radiative properties has been presented elsewhere [10]. Therefore, only a brief overview will be presented here. The fraction of ions in the j^{th} ionization state, f_j, of a given species is determined from the coupled set of rate equations:

$$\left(\frac{df_j}{dt}\right) = n_e \{f_{j-1} C_{j-1}^{coll} - f_j(C_j^{coll} + \alpha_j^{tot}) + f_{j+1}\alpha_{j+1}^{tot}\} \quad j=1,Z , \qquad (1)$$

where Z is the atomic number, n_e is the electron density, C_j^{coll} is the

collisional ionization rate from state j to j+1, and α_{j+1}^{tot} is the sum of the collisional, radiative, and dielectronic recombination rates from state j+1 to j. In the steady-state approximation, $(df_j/dt) = 0$ and the ionization populations are determined by:

$$f_j = \left(\prod_{m=0}^{j-1} R_{m,m+1}\right) / \left(1 + \sum_{l=1}^{z} \prod_{m=0}^{l-1} R_{m,m+1}\right) \tag{2}$$

where

$$R_{m,m+1} = \frac{C_m^{coll}}{\alpha_{m+1}^{coll} + \alpha_{m+1}^{rad} + \alpha_{m+1}^{diel}} .$$

The collisional ionization and recombination coefficients for the transition between ionization states j and j+1 can be written as [11]:

$$C_j^{coll} = (1.09\times10^{-6}\,cm^3s^{-1})T^{1/2} \cdot e^{-\chi_j}(1 - e^{-\chi_j})\Phi_j^{-2}\Gamma_j \tag{3}$$

and

$$\alpha_{j+1}^{coll} = C_j^{coll} \cdot (1.66\times10^{-22})n_eT^{-3/2} \cdot e^{\chi_j}(U_{j+1}/U_j) \tag{4}$$

where T is the electron temperature in eV, Φ_j is the ionization potential in eV, $\chi_j \equiv \Phi_j/T$, Γ_j is the Gaunt factor, and U_j and U_{j+1} are the electronic partition functions for the j^{th} and $(j+1)^{st}$ ionization stages.

For the radiative recombination coefficient, we use the formula derived by Seaton [12]:

$$\alpha_{j+1}^{rad} = (5.20\times10^{-14}\text{cm}^3\text{s}^{-1})(j+1)\chi_j^{3/2} \cdot e^{\chi_j} E_1(\chi_j) \qquad (5)$$

where $E_1(\chi_j)$ is the first exponential integral [13], and a Gaunt factor of unity is assumed.

At relatively high temperatures, dielectronic recombination is often the dominant recombination process. For this, we use the modifications of Post et al. [11] to the formulae originally proposed by Burgess [13]:

$$\alpha_{j+1}^{diel} = (2.40\times10^{-9}\text{cm}^3\text{s}^{-1})T^{-3/2}B(j)D(j) \cdot \sum_n f_{ni}A(y)e^{-\bar{E}_{ni}(j)/T} \qquad (6)$$

where i is the initial electronic state of the ion, and the summation is over all bound states n. f_{ni} is the oscillator strength for the exciting transition. The expressions for B(j) and E(j) are

$$B(z \equiv j+1) = z^{1/2}(z+1)^{5/2}(z^2+13.4)^{-1/2}$$

$$\bar{E}_{ni}(z) = 13.6\ \text{eV}(z+1)^2(\nu_i^{-2} - \nu_n^{-2})/a$$

where

$$a = 1 + 0.015(j+1)^3/(j+2)^2 \ ,$$

and ν_i and ν_n are the effective principal quantum numbers of state i and n, respectively. The formulae for A(y) and D(j) depend on whether a change in the

principal quantum number occurs during the excitation. They are defined as

$$A(y) = \begin{cases} y^{1/2}/(1 + 0.105y + 0.015y^2), & \Delta n = 0 \\ y^{1/2}/(2 + 0.420y + 0.060y^2), & \Delta n \neq 0 \end{cases}$$

$$D(q \equiv j+2) = \begin{cases} N_t/(N_t + 200), & \Delta n = 0 \\ (qN_t)^2/[(qN_t)^2 + 667], & \Delta n \neq 0 \end{cases}$$

where

$$y = (j+2)/(\nu_i^{-2} - \nu_n^{-2})$$

and

$$N_t = [1.51 \times 10^{17} (j+1)^6 T^{1/2}/n_e]^{1/7} .$$

D(q) represents a reduction factor to account for increased collisional effects at high densities.

Both the radiative and dielectronic recombination rates ($n_e n_{j+1} \alpha_{j+1}$) increase linearly with the electron density, while the collisional recombination rate increases as the square of the electron density. This is because collisional recombination is a 3-body process involving two electrons and an ion, whereas radiative and dielectronic recombination are considered to be 2-body reactions with the excess energy being carried off by a photon rather than a second electron. Thus, in the high density limit, $\alpha_{coll} >> \alpha_{rad} + \alpha_{diel}$, and the plasma is in local thermodynamic equilibrium.

The conditions under which a plasma will be in LTE can be determined by comparing the 3-body and 2-body recombination rates. Results for a nitrogen plasma are presented in Figure 2. Here, the ratio of the collisional recombination rate to the sum of the radiative and dielectronic rates is plotted as a function of the ion density for three different electron temperatures: 1, 10, and 100 eV. For each temperature, the recombination rates were computed for the most abundant ionization state: $N^{1+} \rightarrow N^{0+}$ at 1 eV, $N^{4+} \rightarrow N^{3+}$ at 10 eV, and $N^{6+} \rightarrow N^{5+}$ at 100 eV. When $\alpha_{coll} >> \alpha_{rad} + \alpha_{diel}$ (above the dashed line) the plasma is in collisional equilibrium, and the ionization and excitation populations can be accurately computed using the well-known Saha equation and Boltzmann statistics [14]. However, this does not occur until the nitrogen ion density is $\gtrsim 10^{18}$, 10^{19}, and 10^{21} cm^{-3} for temperatures of 1, 10, and 100 eV, respectively.

The densities in ICF target chambers are expected to range between 10^{12} and 10^{19} cm^{-3}, and temperatures from ~ 1 eV to 1 keV. In Figure 2, this range of densities and temperatures is indicated by the shaded region. Hence, it is seen that the background plasma in ICF target chambers cannot be assumed to be in local thermodyanamic equilibrium, as 2-body recombination processes often dominate. On the other hand, it is seen that collisional recombination cannot always be neglected. Thus, both 2-body and 3-body processes must be considered simultaneously to adequately determine the populations and radiative properties of target chamber ICF plasmas.

The more general non-LTE plasma can have a significantly lower specific energy, pressure, and average charge state than one assumed to be in LTE. This is because the inclusion of 2-body processes will cause depopulation of the upper ionization and excitation levels. This is shown in Figures 3 and 4,

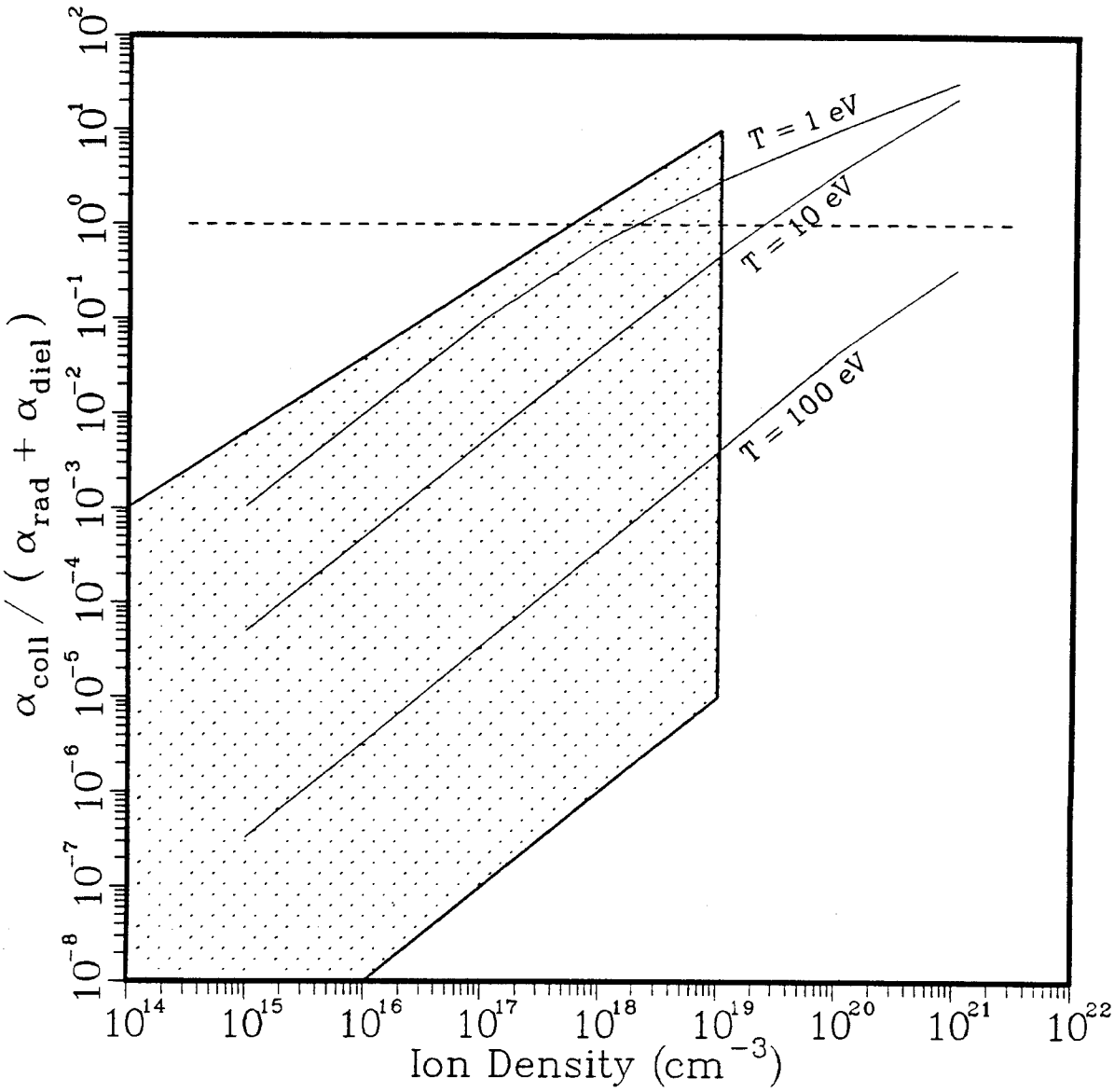

Fig. 2. Ratio of collisional recombination rate to the sum of radiative and dielectronic recombination rates for a nitrogen plasma as a function of density. Results are for the $N^{1+} \rightarrow N^{0}$, $N^{4+} \rightarrow N^{3+}$, and $N^{6+} \rightarrow N^{5+}$ transitions for the 1, 10, and 100 eV curves, respectively. The shaded region represents the regime of densities and temperatures relevant to ICF target chambers.

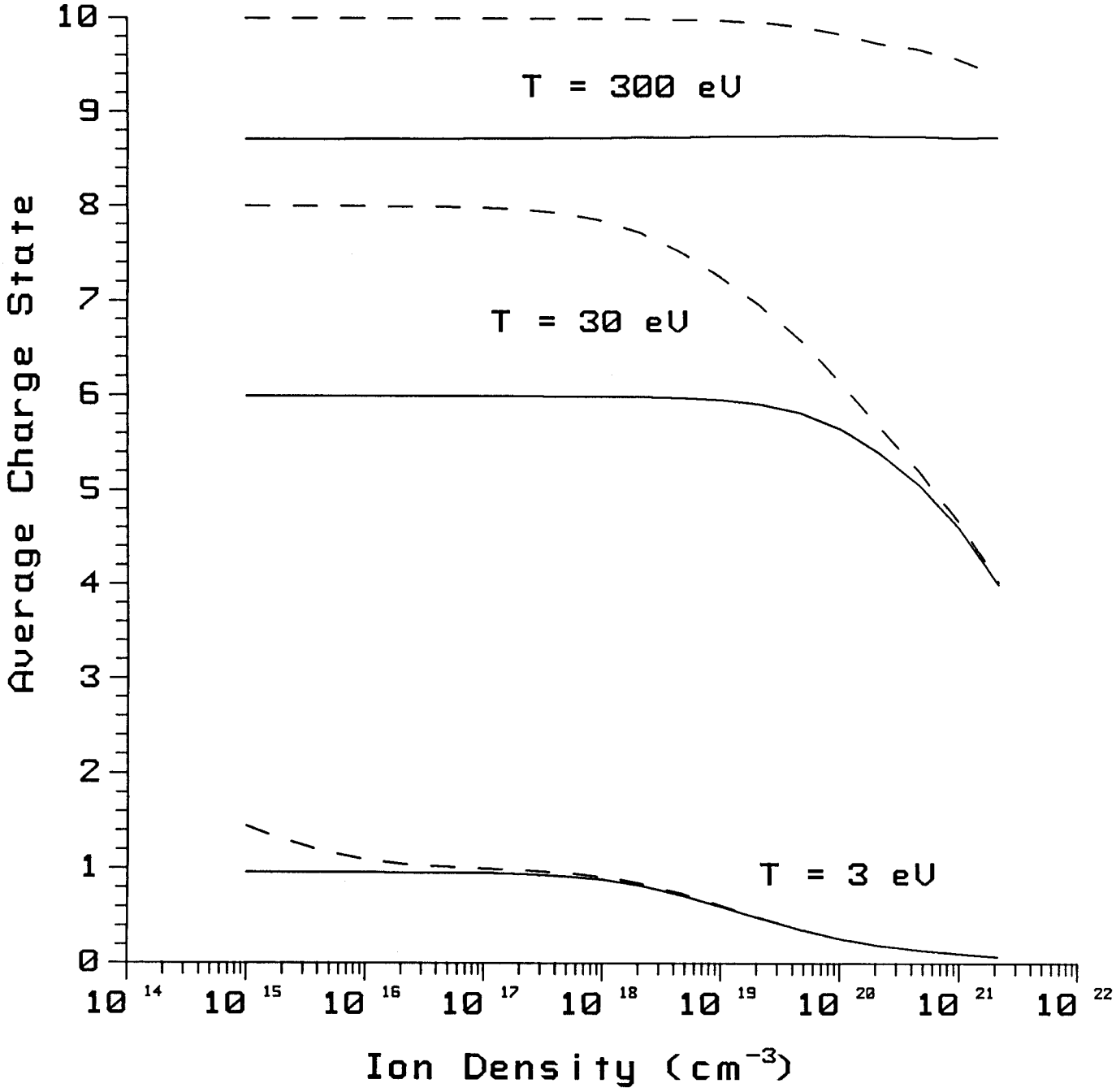

Fig. 3. Average charge state vs. density for neon at temperatures of 3, 30, and 300 eV. Non-LTE processes were included in the calculation of the solid curve. The dashed curve represents results of an LTE plasma.

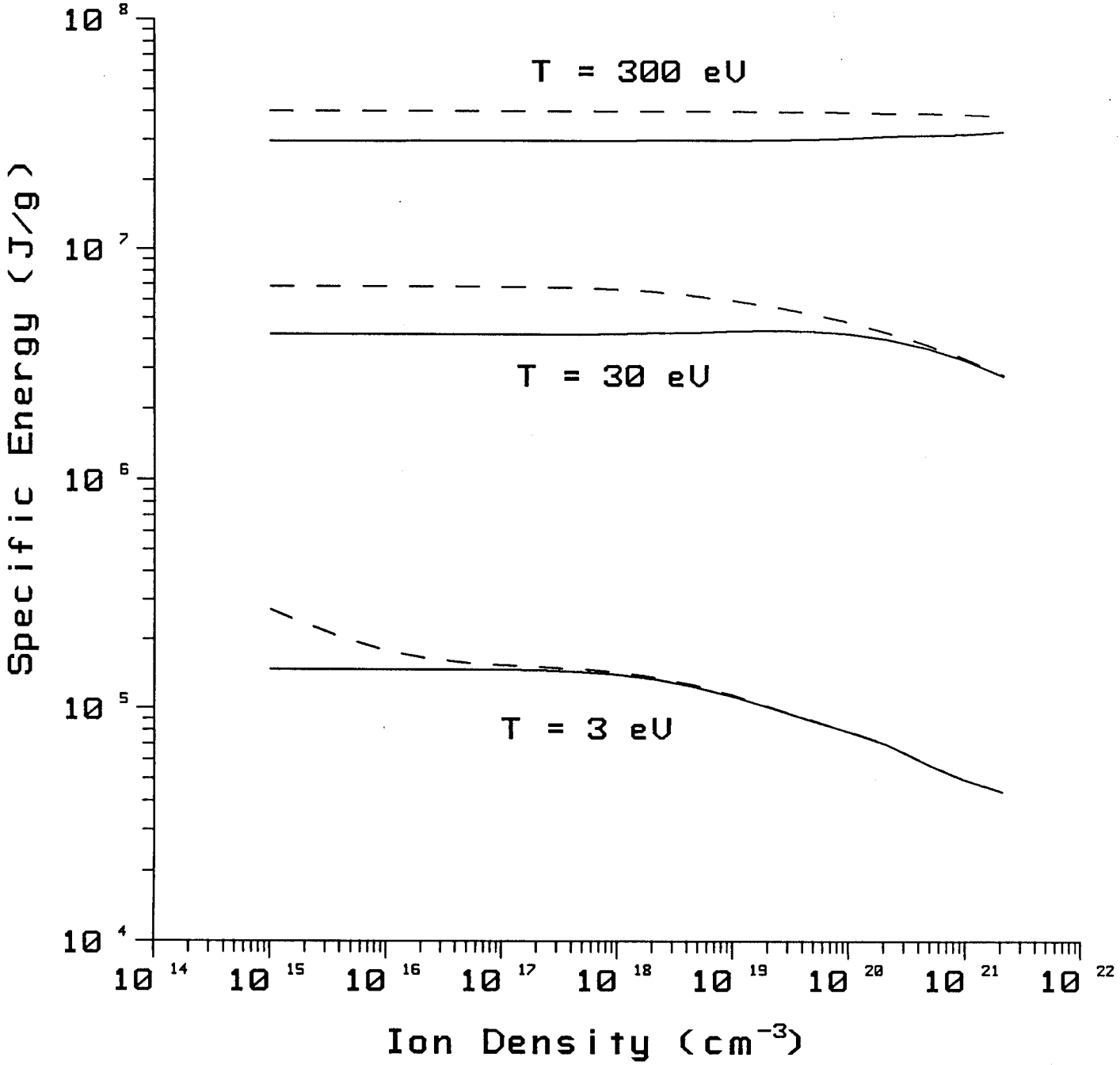

Fig. 4. Specific energy vs. density for neon at temperatures of 3, 30, and 300 eV. Non-LTE processes were included in the calculation of the solid curve. The dashed curve represents results of an LTE plasma.

where the average charge state and specific energy for neon are plotted for three different temperatures as a function of density. The dashed curves in each figure are the results for a plasma assumed to be in LTE. The solid curves represent the more general case where both 2-body and 3-body processes are considered. Again, the transition from the collisionally dominated regime to the radiatively dominated regime shows a strong dependence on the plasma temperature. In Figure 4, it is seen that the assumption of local thermodynamic equilibrium can lead to specific energies that are too large by as much as a factor of two.

It is interesting to consider the evolution of a fluid element as it is heated isochorically from ~ 1 eV to several hundred eV. For a nitrogen plasma with a density of ~ 10^{19} cm^{-3} (see Figure 2), electronic recombination will be collisionally dominated at temperatures ~ 1 eV. As the temperature of the fluid element increases, 2-body recombination becomes more important, and eventually dominates at temperatures $\gtrsim$ 10 eV. At these relatively high temperatures, the plasma is in the so-called "coronal equilibrium" state [8].

The influence of non-LTE processes becomes even more pronounced when calculating the plasma radiative properties. This can be seen by comparing the rates of emission and absorption of photons from a plasma. The general form for the absorption coefficient and emissivity for an ion can be written, respectively, as [8]:

$$\kappa_\nu = \sum_n \sum_{m>n} [N_n - (\frac{g_n}{g_m})N_m]\alpha_{nm}^{bb}(\nu)$$

$$+ \sum_{n>n'} [N_n - N_n^* e^{-h\nu/k_B T}]\alpha_n^{bf}(\nu) + n_e N_+ \alpha^{ff}(\nu)[1 - e^{-h\nu/k_B T}] \qquad (7)$$

and

$$\eta_\nu = \left(\frac{2h\nu^3}{c^2}\right)\left\{\sum_n \sum_{m>n} \left(\frac{g_n}{g_m}\right) N_m \alpha_{nm}^{bb}(\nu) \right.$$

$$\left. + \sum_{n>n'} N_n^* e^{-h\nu/k_B T} \alpha_n^{bf}(\nu) + n_e N_+ \alpha^{ff}(\nu) e^{-h\nu/k_B T} \right\} \qquad (8)$$

where n' is determined by the photoionization cutoff energy, n_e is the electron density, and N_n^* is the equilibrium population of state n calculated using the actual number of ions in the next highest ionization state, N_+. The terms h, c, k_B, and ν as usual represent Planck's constant, the speed of light, Boltzmann's constant, and the photon frequency. The α's and g's represent the cross sections of the various transitions and the degeneracy factors, respectively.

The terms from left to right in Eqs. (7) and (8) represent the contributions from bound-bound, bound-free, and free-free transitions. The second term inside each of the square brackets in Eq. (7) is the contribution from stimulated emission to the absorption coefficient. Note that for high densities (i.e., LTE), $N_m = N_n(g_m/g_n)\, e^{-h\nu_{mn}/k_B T}$ and $N_n = N_n^*$. Thus, the correction for stimulated emission for all three transitions reduces to the LTE form $1 - \exp(-h\nu/k_B T)$, and the relation between the absorption coefficient and emissivity is given by the well-known Kirchoff-Planck relation, $\eta_\nu = \kappa_\nu B_\nu$ (where B_ν is the Planck function).

The ratio of the average absorption to emission rate is determined by integrating Eqs. (7) and (8) over all frequencies to get the Planck means:

$$\sigma_P^A \,/\, \sigma_P^E = \left[\int_0^\infty d\nu\, \kappa_\nu B_\nu\right] \,/\, \left[\int_0^\infty d\nu\, \eta_\nu\right] . \qquad (9)$$

This ratio is plotted in Figure 5 for a neon plasma as a function of density for three temperatures. Again, at relatively low temperatures and high densities, the plasma is in LTE. But at temperatures $\gtrsim 10^2$ eV, plasmas at densities $\lesssim 10^{21}$ cm^{-3} are very far from LTE. Thus, at densities relevant to ICF target chambers, the non-LTE plasma emission rate can be several orders of magnitude lower than that calculated assuming LTE. And as we will show below, this lower emission rate for non-LTE plasmas can lead to a significantly lower radiation flux and stronger shock wave in the target chamber background plasma.

3. APPLICATION TO ICF TARGET CHAMBERS

In this section, we examine the influence of non-LTE processes on the radiation and hydrodynamic energy transport in ICF target chamber plasmas. To study these effects, we use a one-dimensional Lagrangian radiation-hydrodynamics code [15,16]. Spherical symmetry is assumed. Radiation is transported in 20 photon energy groups using a flux-limited diffusion model, and electron conduction in the background plasma is calculated using Spitzer conductivities [17].

Energy from the target is deposited into the background gas using time-dependent debris ion and energy-dependent x-ray deposition models. In the calculations discussed below, the target x-ray and debris ion yields are 150 MJ and 50 MJ, respectively. The target x-ray spectrum is based on target burn calculations [18] using the PHD-IV radiation-hydrodynamics code [19], and is shown in Figure 6. The debris ions expand isotropically from the explosion point source at a constant rate during the first 100 ns of each simulation.

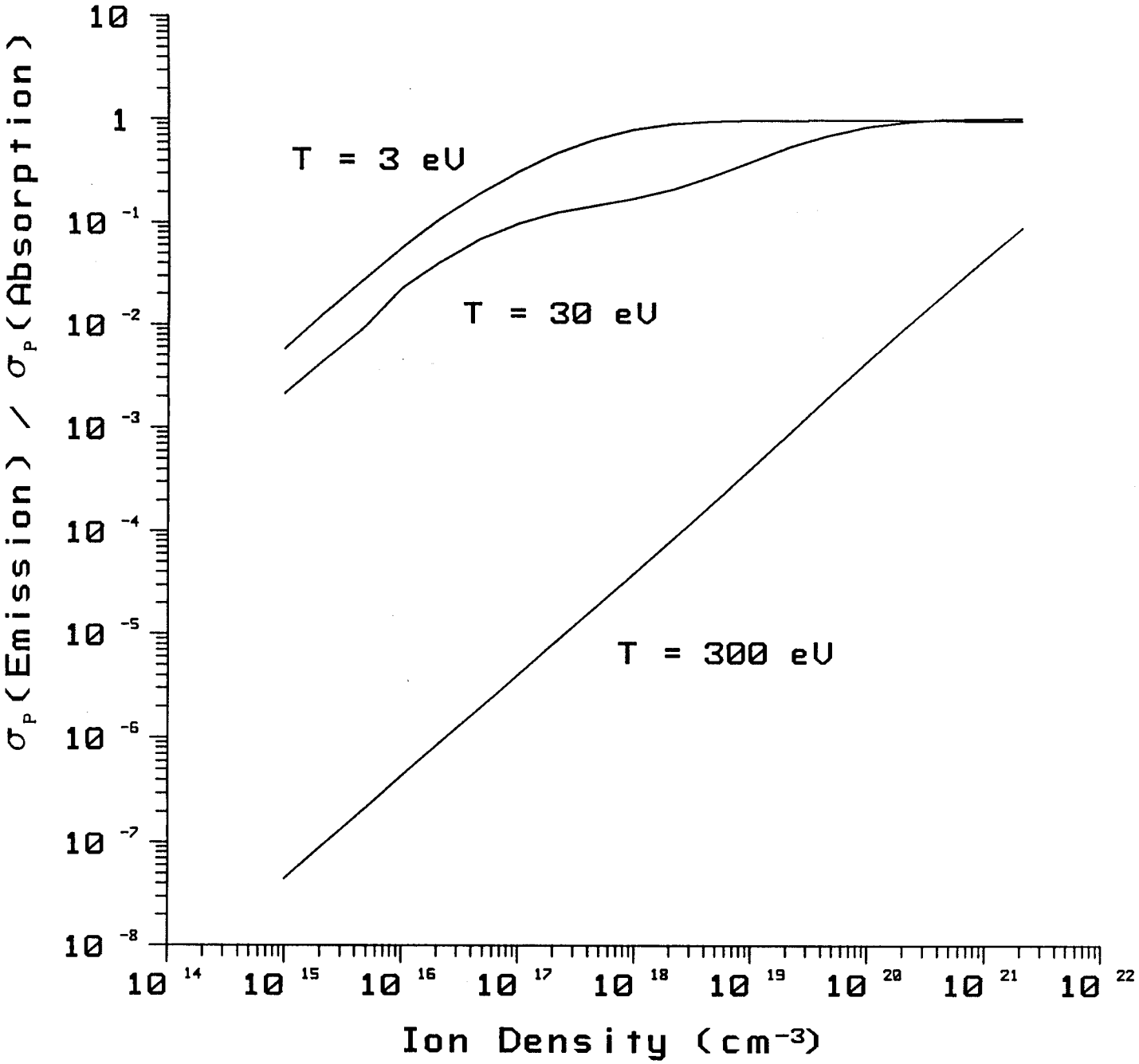

Fig. 5. Ratio of the Planck mean absorption and emission rates for neon vs. density for temperatures of 3, 30, and 300 eV.

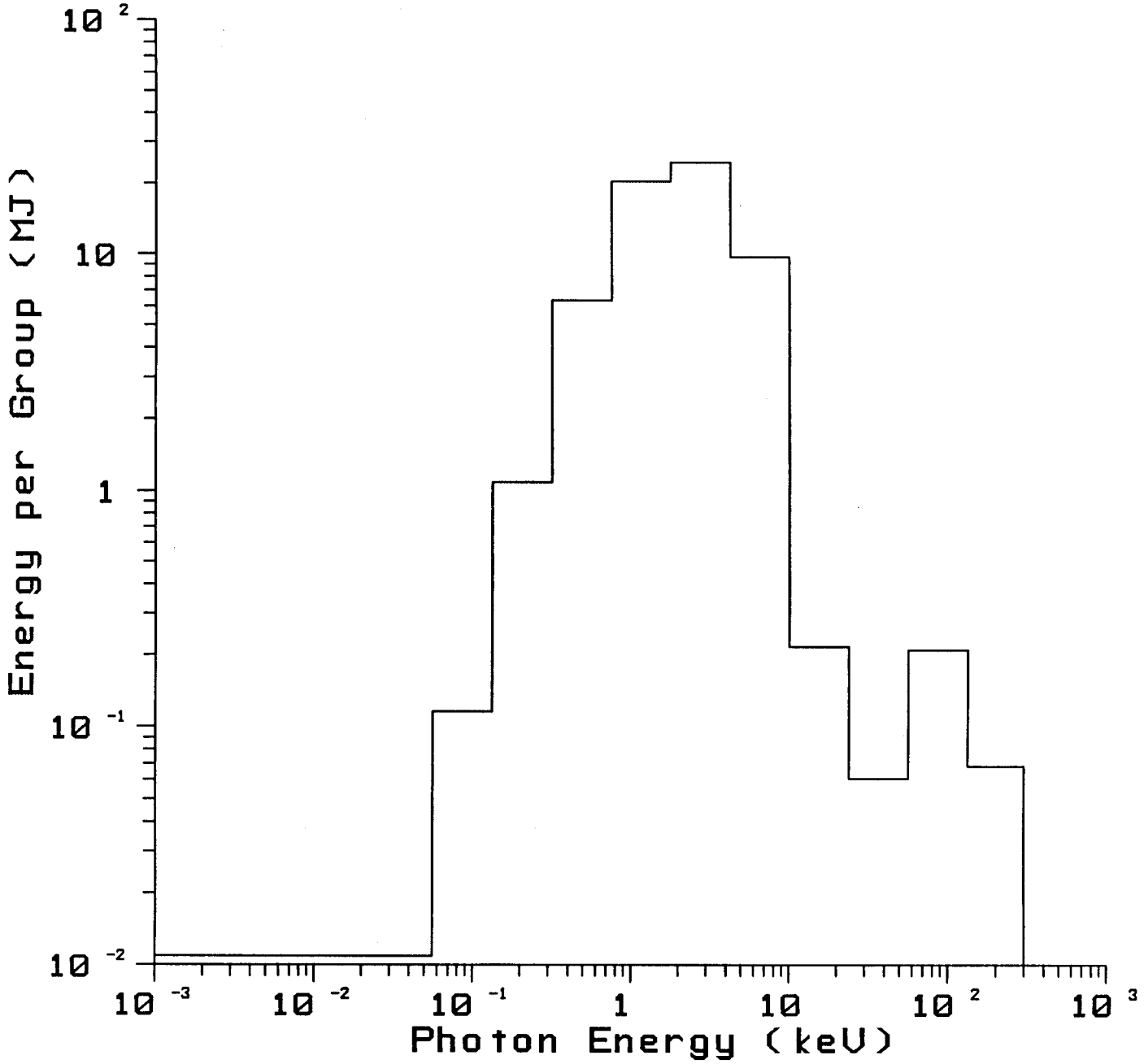

Fig. 6. Target x-ray spectrum for radiation-hydrodynamic simulations.

The initial properties of debris ions are listed in Table 1. The debris ions transfer momentum and energy to the background plasma via ion-atom, ion-electron, and ion-ion collisions. The rate of energy loss by the debris ions is computed using a stopping power model which includes high temperature effects (i.e., free electron-ion collisions), and is described in detail elsewhere [20].

Table 1. Target Debris Ion Energies

Debris Ion	Initial Kinetic Energy	Total Energy (MJ)
Deuterium	1.9 keV/particle	0.082
Tritium	2.9 keV/particle	0.122
Helium	3.8 keV/particle	0.070
Lithium	6.6 keV/particle	1.89
Lead	198 keV/particle	23.9

The target chamber radius in these calculations is varied between 1 and 3 meters, and the background gas is composed of pure argon. For background gas densities $\gtrsim 10^{17}$ cm^{-3}, the debris ions deposit their energy within several centimeters of the target. On the other hand, the photon mean free paths of the target x-rays are often considerably longer, and a significant fraction of their energy will not be absorbed by the background gas.

Figure 7 shows the radiation flux as a function of time at the grid boundary (which represents the chamber wall) located 3 meters from the target. In this calculation, the background gas initially has a uniform density of 3.55×10^{15} cm^{-3}, corresponding to a pressure of 0.1 torr at room temperature. The solid curve represents the results obtained using an argon equation of state and opacities in which non-LTE processes are considered. For comparison, the dashed line shows the flux calculated using a strictly LTE equation

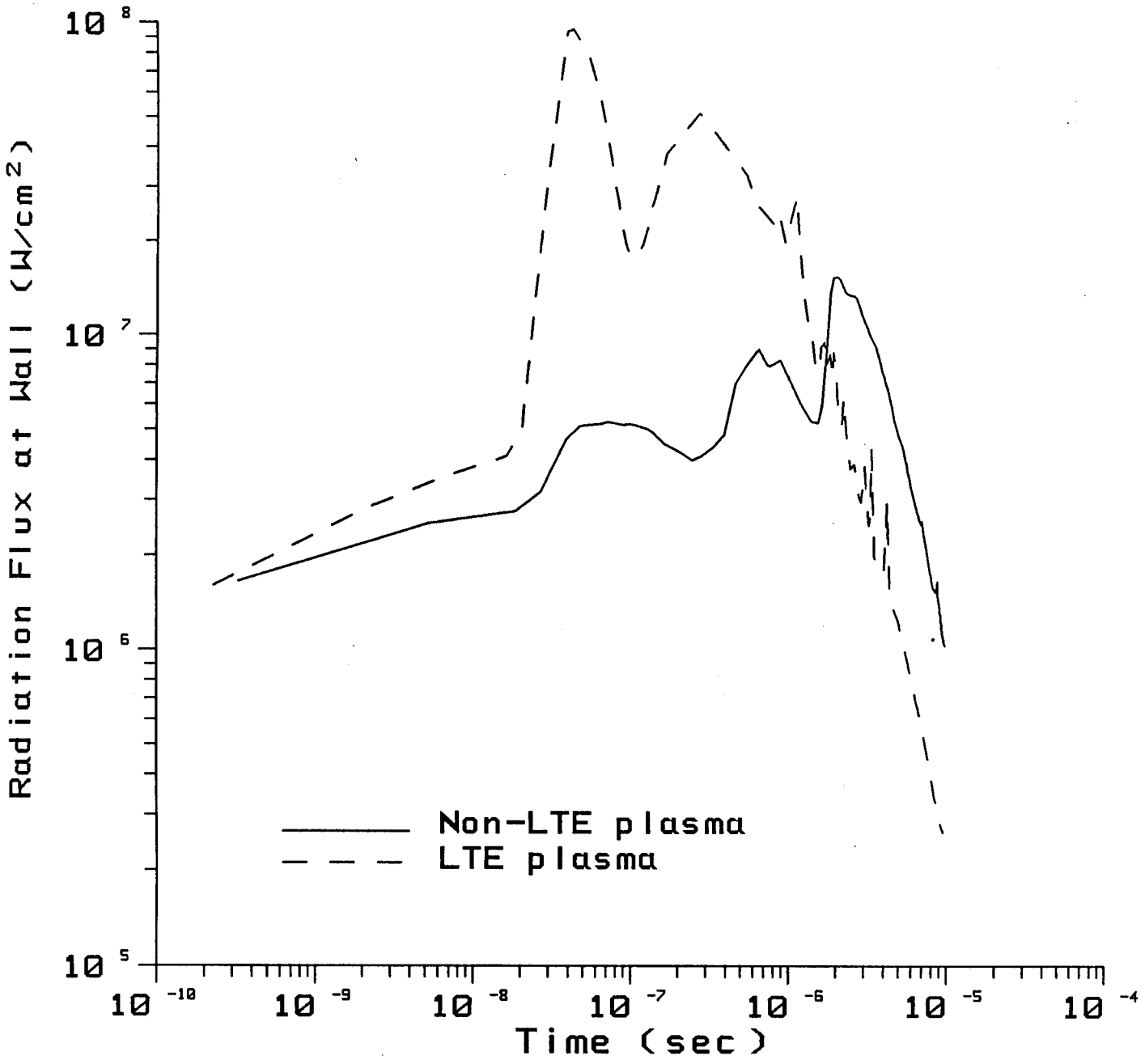

Fig. 7. Radiation flux vs. time at a surface located 3 meters from the target. The background plasma is argon and has an initial density of 3.55×10^{15} cm^{-3}.

of state and opacities. Including non-LTE effects in the background plasma tends to reduce the flux by roughly an order of magnitude. This is due to the fact that radiative deexcitation decreases the fraction of excited state ions, which in turn reduces the plasma emission rate. In the LTE case, the flux drops rapidly after ~ 2 μs because there is very little energy remaining in the plasma.

The time-integrated flux at 3 meters is shown in Figure 8. Again, the non-LTE plasma is seen to lose its energy at a much slower rate. In this calculation, the total energy absorbed by the background plasma from the x-rays and debris ions was 72 MJ. Thus, at a distance of 3 meters, the plasma has lost all of its energy when the energy radiated to the wall reaches 64 J/cm^2.

Because of the lower non-LTE plasma emission rates, the microfireball will retain its thermal energy for a longer period of time. This is shown in Figure 9, where the temperature at the center of the microfireball is plotted as a function of time. In both the LTE and non-LTE cases, the temperatures reach a maximum of several keV at ~ 10^{-1} μs as the debris ions deposit their energy. The central temperature calculated using non-LTE plasma properties remains above 100 eV out to ~ 10 μs. On the other hand, when non-LTE processes are neglected, the central temperature is predicted to decrease rapidly down to < 10 eV at ~ 5 μs.

Figure 9 clearly illustrates the importance of non-LTE processes in the background plasma following an inertial fusion target explosion. These processes will especially need to be considered in the interpretation of diagnostic data from high-gain target experiments, such as those envisioned for the Laboratory Microfusion Facility [21]. Non-LTE effects may also be

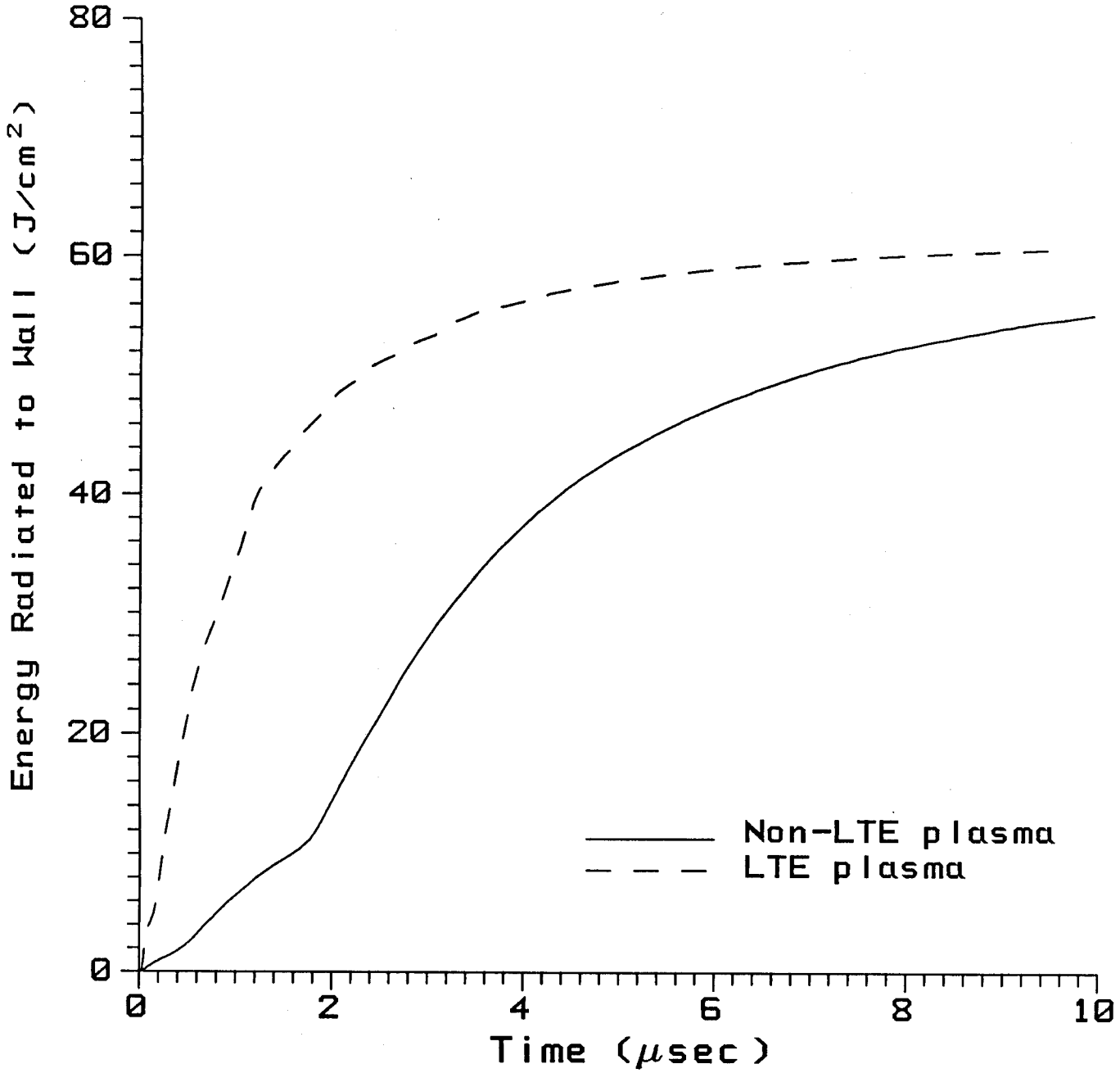

Fig. 8. Time-integrated energy radiated to a surface located 3 meters from the target vs. time. The background plasma is argon and has an initial density of 3.55×10^{15} cm^{-3}.

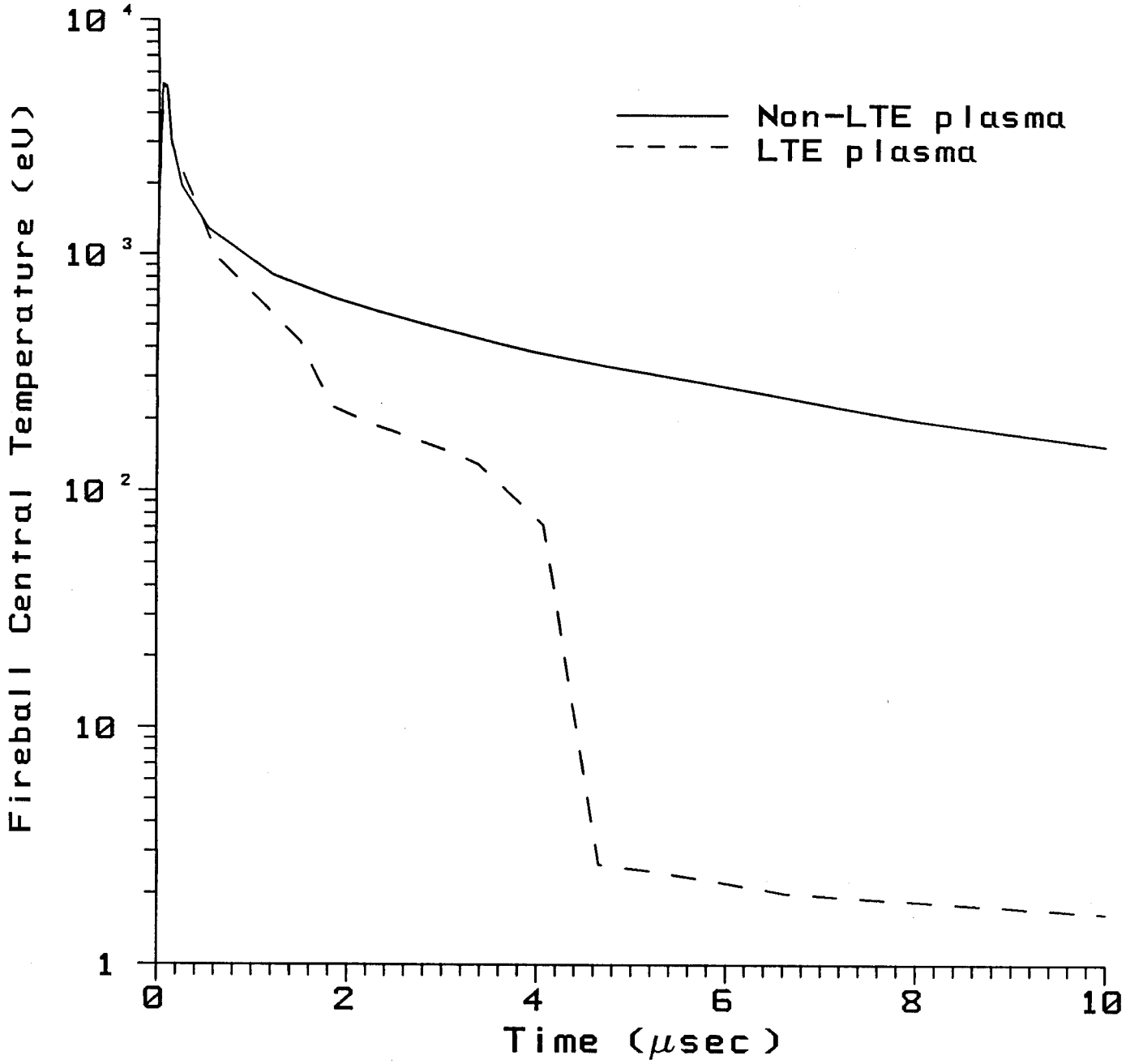

Fig. 9. Temperature at the center of the microfireball vs. time. Non-LTE processes were included in the calculation of the solid curve. The dashed curve represents results of an LTE plasma.

important in target chambers with low density ($\lesssim 10^{14}$ cm^{-3}) background gases. In this situation, material ablated from the wall by target x-rays will interact with the later arriving target debris ions. This vapor could then be heated to temperatures ~ 10 to 10^2 eV, producing a non-LTE plasma. Thus, non-LTE effects will be important for a variety of processes associated with inertial fusion target explosions.

The lower emission rate of non-LTE plasmas also produces a stronger shock front emanating from the target. Figure 10 shows the pressure at a surface located 1 meter from the target as a function of time. In this problem, the initial background gas density was 3.55×10^{16} cm^{-3}, corresponding to a pressure of 1 torr at room temperature. The pressure determined using non-LTE plasma properties is represented by the solid curve. The dashed curve represents the pressure calculated using an LTE equation of state and opacities. For comparison, the dotted line in Figure 10 represent the results from a calculation in which the plasma neither emitted nor absorbed radiation -- i.e., a pure hydrodynamics calculation.

In the non-LTE calculation, the average shock velocity (as determined by the arrival time at 1 meter), is almost twice as fast as the shock in the LTE case. Also, the peak pressure at 1 meter is seen to be roughly an order of magnitude higher in the non-LTE case. In the calculation with no plasma emission, the average shock velocity is more the twice as fast as in the non-LTE calculation and four times faster than the LTE shock. This is because as the plasma behind the shock retains more of its thermal energy, the pressure behind the shock front remains higher and there is more energy available to perform work ($P \cdot dV$) on the blast wave.

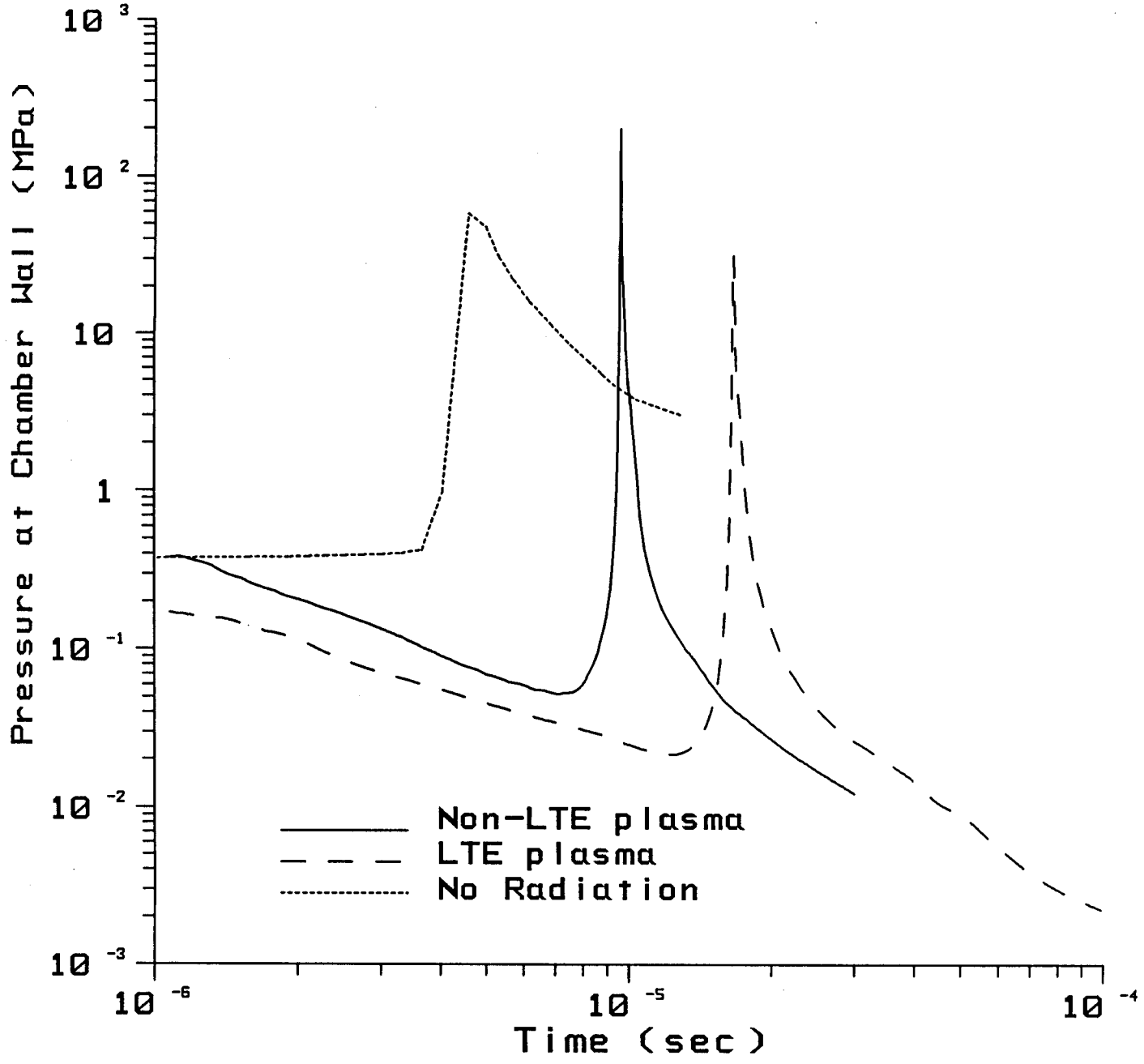

Fig. 10. Pressure at a surface located 1 meter from the target vs. time. The background plasma is argon and has an initial density of 3.55×10^{16} cm^{-3}.

The shock-produced impulse at the surface in these calculations is 18, 11, and ~ 100 Pa-s for the non-LTE, LTE, and "no radiation" cases, respectively. Clearly, radiation effects play a significant role in reducing the strength of the shock as it expands away from the target. However, the shock-generated impulse can be noticeably underestimated if the plasma properties are based on LTE assumptions. Determining the strength of the shock is critical because impulses of this magnitude are capable of inflicting an unacceptable level of damage to the chamber structure. Because of this, the shock properties play a major role in the designs of ICF target chambers.

4. CONCLUSIONS

We have calculated the equations of state and radiative properties of plasmas over a range of densities and temperatures relevant to ICF target chamber applications, and which encompass the transition between the LTE and non-LTE plasma regimes. It was found that for plasma densities of ~ 10^{18}, 10^{19}, and 10^{21} cm^{-3}, 2-body (non-LTE) atomic processes dominate at temperature $\gtrsim$ 1, 10, and 100 eV, respectively. At densities < 10^{17} cm^{-3} collisional recombination and deexcitation are unimportant and the assumption of local thermodynamic equilibrium is invalid at all temperatures $\gtrsim$ 1 eV. Non-LTE processes in low density plasmas produce a relative depopulation of the excited states of ions, which in turn can significantly reduce the plasma emission rate.

Numerical simulations of ICF target chamber environments indicate that the background plasma will often -- though not always -- be dominated by non-LTE atomic processes. For target chambers with relatively high density

background gases ($\gtrsim 10^{17}$ cm^{-3}), both 2-body (radiative) and 3-body (collisional) recombination and deexcitation processes must be fully considered when calculating equation of state and radiative properties of a plasma. The lower (relative to LTE) plasma emission rates can result in: (1) the microfireball retaining its thermal energy for a longer period of time; (2) a more energetic blast wave capable of producing a stronger impulse at the chamber wall; and (3) a lower radiation flux at the chamber wall, which can potentially reduce the amount of material vaporized from the wall. In addition, non-LTE processes must be considered when material vaporized from the chamber wall is heated by the target debris ions. Thus, non-LTE processes are predicted to play a major role in a variety of ICF target chamber phenomena.

ACKNOWLEDGEMENT

Support for this work has been provided by Lawrence Livermore National Laboratory. Computing support has been provided by the National Science Foundation through the San Diego Supercomputer Center.

REFERENCES

[1] J.J. Duderstadt and G.A. Moses, Inertial Confinement Fusion (Wiley Interscience, New York, 1982).

[2] K.A. Brueckner, Power Convers. Int. 7 (1981) 76.

[3] C.D. Orth, Fusion Tech. 10 (1986) 1245.

[4] R.R. Peterson, Fusion Tech. 13 (1988) 279.

[5] SIRIUS-M Group, University of Wisconsin Fusion Technology Institute Report UWFDM-711 (1986); LIBRA Group, University of Wisconsin Fusion Technology Report UWFDM-754 (1988).

[6] M. Uesaka, R.R. Peterson, and G.A. Moses, Nucl. Fusion 24 (1984) 1137.

[7] L.A. Glenn, Nucl. Eng. and Design 54 (1979) 1.

[8] D. Mihalas, Stellar Atmospheres (W. H. Freeman, San Francisco, 1978).

[9] Y.B. Zeldovich and Y.P. Raizer, Physics of Shock Waves and High-Temperature Hydrodynamic Phenomena (Academic Press, New York, 1966).

[10] J.J. MacFarlane, University of Wisconsin Fusion Technology Institute Report UWFDM-750 (1987), submitted to Comput. Phys. Commun.

[11] D.E. Post, R.V. Jensen, C.B. Tarter, W.H. Grasberger, and W.A. Lokke, At. Data Nucl. Data Tables 20 (1977) 397.

[12] M.J. Seaton, Mon. Not. R. Astr. Soc. 119 (1959) 81.

[13] A. Burgess, Astrophys. J. 141 (1965) 1588.

[14] See, e.g., D.A. McQuarrie, Statistical Mechanics (Harper and Row, New York, 1976)

[15] G.A. Moses, R.R. Peterson, and T.J. McCarville, Comput. Phys. Commun. 36 (1985) 249.

[16] R.R. Peterson and G.A. Moses, University of Wisconsin Fusion Technology Institute Report UWFDM-670 (1986).

[17] L. Spitzer, Physics of Fully Ionized Gases, Second Edition (Interscience, New York, 1966).

[18] HIBALL Group, University of Wisconsin Fusion Technology Institute Report UWFDM-450 (1981).

[19] G.A. Moses, G.R. Magelssen, R. Israel, and T. Spindler, University of Wisconsin Fusion Technology Institute Report UWFDM-194 (revised 1982).

[20] J.J. MacFarlane, G.A. Moses, and R.R. Peterson, University of Wisconsin Fusion Technology Institute Report UWFDM-723 (1987).

[21] W.J. Hogan, Bull. Amer. Phys. Soc. 32 (1987) 1788.